Accepted Manuscript

Lysine assisted hydrothermal synthesis and formation process of $MoO_3:Sm^{3+}$ phosphors with hierarchical structures and its electron trapping luminescence properties

H.S. Yogananda, R.B. Basavaraj, Ramachandra Naik, G.P. Darshan, S.C. Sharma, Daruka Prasad, H. Nagabhushana

PII: S0925-8388(18)32625-2

DOI: 10.1016/j.jallcom.2018.07.124

Reference: JALCOM 46840

To appear in: *Journal of Alloys and Compounds*

Received Date: 11 April 2018

Revised Date: 9 July 2018

Accepted Date: 10 July 2018

Please cite this article as: H.S. Yogananda, R.B. Basavaraj, R. Naik, G.P. Darshan, S.C. Sharma, Daruka Prasad, H. Nagabhushana, Lysine assisted hydrothermal synthesis and formation process of $MoO_3:Sm^{3+}$ phosphors with hierarchical structures and its electron trapping luminescence properties, *Journal of Alloys and Compounds* (2018), doi: 10.1016/j.jallcom.2018.07.124.

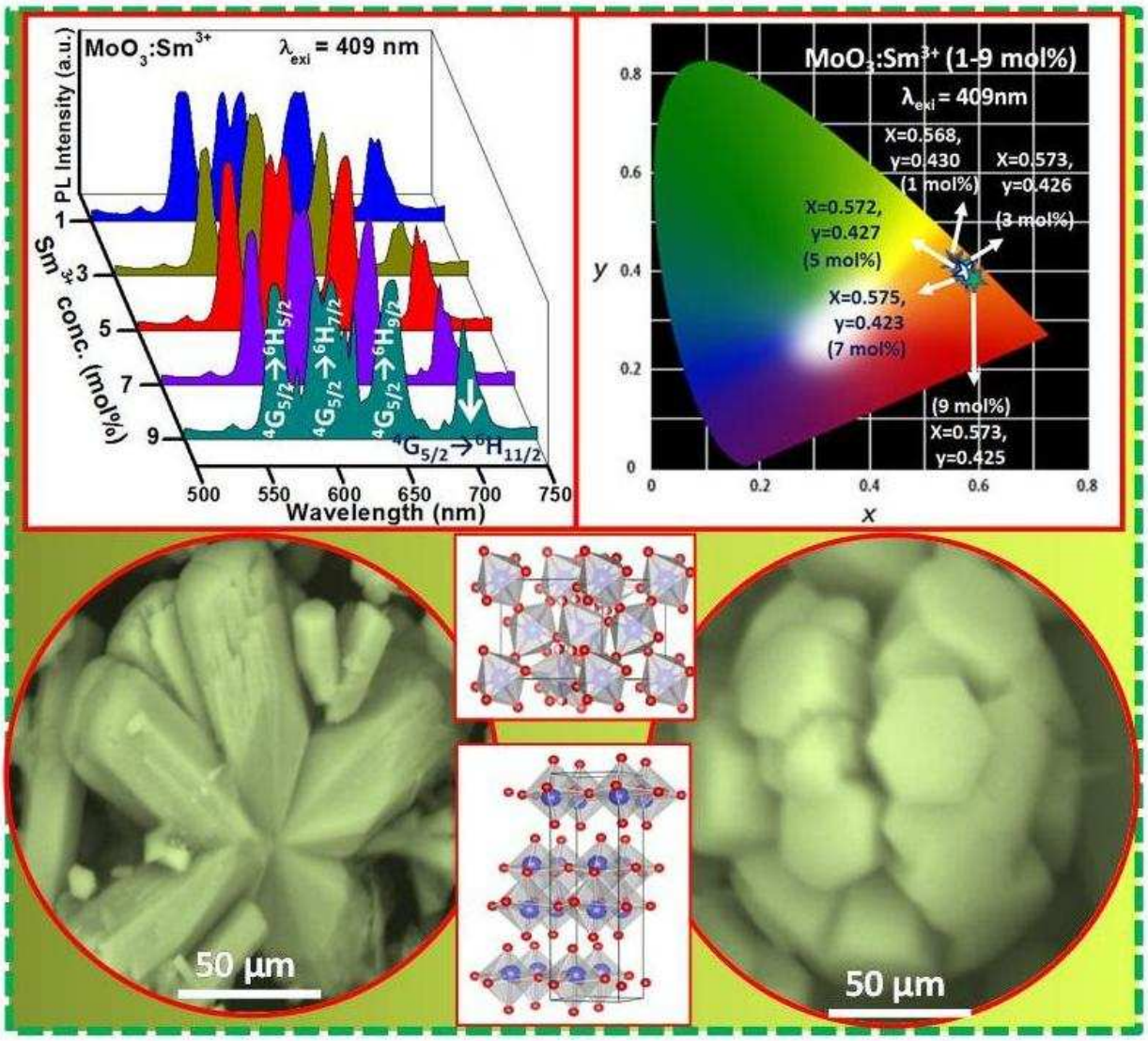

Graphical abstract

Lysine assisted hydrothermal synthesis and formation process of $MoO_3:Sm^{3+}$ phosphors with hierarchical structures and its electron trapping luminescence properties

H.S. Yogananda[1, 2], R.B. Basavaraj[3], Ramachandra Naik[4], G.P. Darshan[5], S.C. Sharma[6], Daruka Prasad[7], H. Nagabhushana[3, *]

[1]Department of Physics, SaiVidya Institute of Technology, VTU, Bangalore 560064, India
[2]Research and Development Center, Bharathiar University, Coimbatore 641046, India
[3]Prof. C.N.R. Rao Centre for Advanced Materials Research, Tumkur University, Tumkur 572 103, India
[4]Department of Physics, New Horizon College of Engineering, Bangalore, 560103, India
[5]Department of Physics, Acharya Institute of Graduate Studies, Bangalore 560 107, India
[6]Honarary Professor, Jain group of Institutions, Bangalore- 560069, India
[7]Department of Physics, B M S Institute of Technology, Bangalore-560064, India

Abstract

We report the synthesis of Sm^{3+} doped MoO_3 nanostructures (NSs) effectively by hydrothermal route using lysine as surfactant. The hexagonal and orthorhombic phases were confirmed by means of Powder X-ray diffraction (PXRD) results. The effect of hydrothermal reactions, such as reaction temperature, surfactant concentration, pH value on the morphology was studied in detail by utilizing scanning electron microscopy (SEM) results. Optical properties of the Sm^{3+} (1- 9 mol %) doped MoO_3 were studied by means of diffuse reflectance spectroscopy (DRS). The 4f-4f emission bands of Sm^{3+} ions were observed at 563, 610, 647 and 698 nm attributed to $^4G_{5/2}$–^6H_J (J = 5/2, 7/2, 9/2, 11/2) of Sm^{3+} respectively under 405 nm ($^6H_{5/2}$→$^4F_{5/2}$ + $^4M_{7/2}$) excitation. Judd–Ofelt theory was utilized to calculate the, transition probabilities (A_T), radiative lifetime (τ_{rad}), branching ratio (β), and asymmetric ratio (A_{21}) by using the intensity parameters. The average quantum efficiency and color purity values of the prepared samples were found to be ~ 79.61% and 97 % respectively. The CIE color coordinates confirmed that the phosphor emits orange-red light, which were quite useful for the fabrication of white light emitting diodes.

Keywords: Hydrothermal; Photometric properties; Judd-Ofelt; Photoluminescence.

*Corresponding Author: E-mail address: bhushanvlc@gmail.com (Dr. H. Nagabhushana).

1. Introduction

Rare earth ions (REI) have been broadly utilized as activators for diverse phosphors. Lanthanide ions (Ln^{3+}) exhibit the characteristic intra 4f-4f transitions owing to its sharp emission peaks [1]. Further, Trivalent samarium (Sm^{3+}) ionsexhibitnarrow band emissions, long lifetimes and large Stokes shifts. The emission intensity and splitting of spectral lines provide a valuable data concerning the nearby site symmetry, sizes of cations and properties of the chemical bonding [2].

In recent years, metal molybdates have attracted much attention owing to their key applications in the fields of optic fiber, catalysts, humidity sensor, display devices and solid-state lasers [3-5]. Due to their excellent band-gap excitation transition-metal oxides exhibit superior photochromic properties and find possible applications in the fields of light emitting diode, sensors and high-density storage devices [6]. Among numerous transition-metal oxides, molybdenum trioxide (MoO_3) is considered as one of the outstanding n-type semiconductors [7]. Moreover, photochromic properties of MoO_3 offer potential applications in optical storage systems, display devices, and smart windows due to its great apparent coloration efficiency under light excitation [8].In this manner, MoO_3 is attracting growing attention.

Till date anumerous methods namely, thermal evaporation, template synthesis, chemical synthesis, sputtering and hydrothermal techniques were proposed to tune the structure and morphology of the MoO_3 product [9-12]. Among the existing synthesis techniques, hydrothermal route considered to be an effective and simple procedure to create new hierarchical structures with controlled morphology. The hexagonal structure of MoO_3 is remarkably interesting owing to its one dimensional (1D) tunnel structure, which results in predominant superior photo-physical and photo-chemical properties in contrast with other MoO_3 structures (orthorhombic and monoclinic) [13-15].

In the present work, dual phased Sm^{3+} doped MoO_3 structures were prepared by simple hydrothermal method using lysine as surfactant. Further, the effect of various reaction conditions on the morphology of the product was studied in detail. Photoluminescence properties were studied in detail in order to utilize the optimized product in solid state lighting applications.

2. Experimental

Simple hydrothermal route has been used to fabricate Sm^{3+} doped MoO_3 nanostructures (NSs). In this route all the chemicals were of analytical grade and used without further purification. Stoichiometric amounts of Ammonium heptamolybdate [$(NH_4)_6Mo_7O_{24}\cdot 4H_2O$; Sigma Aldrich], formic acid [HCOOH], nitric acid [HNO_3] and lysine [$C_6H_{14}N_2O_2$; Sigma Aldrich] were dissolved in 30 mL deionized water with continuous stirring. The obtained reaction mixture was then transmitted to a autoclave (50 mL) and heat treatedat 120 ^oC for 24 h in hot air oven. And thereafter, the autoclave was allowed to cool at room temperature (RT). The final product was thoroughly washed with several times using ethanol and water in order to remove the impurities and finally dried at 60 ^oC for 24 h in vacuum oven. Further, morphology of the product was varied with different hydrothermal reaction conditions. The schematic diagram for the synthesis MoO_3:Sm^{3+} NSs was shown in Fig. 1.

2.1 Instruments used

The X-ray powder diffractometer (Shimadzu made X-ray diffractometer (PXRD-7000) with nickel filter and Cu-K_α radiation (λ = 0.15406 nm) is used for phase purity. Morphological features were observed by scanning electron microscope (SEM, Model No. Hitachi-7000 model) and transmission electron microscope (TEM, Model No. Hitachi H-8100 with accelerating voltage up to 200 KV). The Jobin-Yvon made Flurolog-3 Spectrofluorimeter with 450 W Xenon lamp as an excitation source is used to record photoluminescence (PL) data. PerkinElmer (Lambda-35) spectrometer was used to record the diffuse reflectance spectroscopic data of the NSs.

3. Results and discussion

3.1 PXRD analysis

The powder X-ray diffraction (PXRD) patterns of MoO_3 fabricated via hydrothermal route and calcined at 120 ^oC and 240 °C respectively (Fig. 2(a)). The product calcined at 120 ^oC corresponds to orthorhombic α-MoO_3 phase (JCPDS.No.35-0609). However, when the product calcined at 240°C corresponds to hexagonal phase of MoO_3 (JCPDS.No. 21-0569) [16]. PXRD was utilized to calculate the peak broadening with crystallite size and lattice strain due to dislocation [17]. The crystallite size of the α-MoO_3 and h-MoO_3 NSs were estimated by the X-ray line broadening using Scherrer's equation;

$$D = \frac{k\lambda}{\beta \cos\theta} \text{ ---------- (1)}$$

Where, D; crystallite size, λ; wavelength of the X-rays used (1.54056 Å), k; constant (0.94), β; full width at half-maximum, and θ; peak position. The breadth of the Bragg peak is a combination of both instrumentas well as sample. To combine these contributions, it is essential to collect a diffraction pattern from the line broadening of a standard sample. In the present case silicon was used as a standard sample to estimate the instrumental broadening. The instrument-corrected broadening [18] β corresponding to the diffraction peak of MoO_3 was estimated using the relations;

$$\beta^2 = \left[\left(\beta^2\right)_{measured} - \beta^2{}_{instrumental}\right] \Rightarrow \text{ ------- (2)}$$

$$D = \frac{k\lambda}{\beta \cos\theta} \Rightarrow \cos\theta \frac{k\lambda}{D}\left(\frac{1}{\beta}\right) \quad \text{------- (3)}$$

The estimated values were found to be 40 nm and 26 nm for α-MoO_3 and h-MoO_3 NSs respectively. Further, strain-induced broadening arising from crystal imperfections and distortion were related by $\varepsilon \approx \beta_s / \tan\theta$. A 1/cosθ dependency in W-H plots does not follow tan θ presented in Scherrer's relation. This modification allows crystallite size as well as micro-strainoccurs together. The assorted techniques available in the accompanying expect that size and strain widening were added components of the total integral broadness of a Bragg peak.

The distinctive θ dependencies of both methods set on the basis of size and strain widening in the examination of W-H (Fig. 2 (b)). By combining the Scherrer's relation and $\varepsilon \approx \beta_s / \tan\theta$, which results in [19];

$$\beta_{hkl} = \beta_s + \beta_D \text{ --------- (4)}$$

$$\beta_{hkl} = \left(\frac{k\lambda}{D\cos\theta}\right) + (4\varepsilon \tan\theta) \text{ ---------- (5)}$$

Where β; FWHM (rad), θ; Bragg's angle, λ; wavelength of X-rays, 'D'; crystallite size and ε; the micro strain. The strain and the crystallite size were estimated from the slope and the

intercept respectively. The crystallite size and strain values obtained by W-H plots were found to be 43 nm, 33 x 10^{-4} for α -MoO_3 and 30 nm, 53 x 10^{-4} for h-MoO_3 phase respectively. From the results it was observed that for α -MoO_3 and h- MoO_3, a small variation in crystallite size obtained from both Scherrer's as well as W-H plots.

3.2 Morphological analysis

Fig. 3 (a- d) shows the SEM images of α-MoO_3 obtained at different temperatures (120 ^oC to 240 ^oC for 24 h). It was evident from the figure that the temperature greatly affects the morphology of the samples. When the temperature was set to 120 and 160 ^oC, the product composed of various uneven sized needles shaped structures. However, when the temperature maintained at 180 ^oC, the product composed of bigger and smaller sized rod-like structures. When the temperature was set to 240 ^oC uneven, agglomerated free smooth rods were obtained.

Further, the effect of lysine concentration on α phase was studied by maintaining the temperature at 120 ^oC for 24 h and shown in Fig. 4(a-f). From the figure it was observed that a flaky morphology was obtained for 0.5 and 1 g of lysine (Fig.4a, b). However, when the concentration of lysine was maintained at 1.5 and 2 g, these flakes were oriented in a particular direction (Fig.4 c, d). When the concentration was maintained at 2.5 and 3 g, the oriented flaky type rods assembled together and form clusters (Fig.4e, f). Further, the concentration of lysine was also extended on h-phase by maintaining at 240 ^oC for 24 h (Fig.5a-f). From the figure it was observed that flakes as well as rod-like structures were obtained for 0.5 and 1 g of lysine (Fig.5a, b). However, 1.5 - 3 g of lysine treated samples exhibit individual smooth hexagonal rods (Fig.5c-f). Effect of hydrothermal reaction duration on the morphology was studied for optimized conditions at 240 ^oC and 3 g of lysine (Fig. 6 a-d). As can be seen from the figure fiber-like structures were obtained for 4 and 8 h (Fig.6a & b). However, when the hydrothermal duration was set to 12 h, the product composed of combination of fibers as well as rods (Fig.6c). For 16 h time duration, fiber like structures was disappeared and form sharp tipped rods and flakes (Fig.6d).

In the absence of lysine surfactant, the reduction of surface energy leads to the anisotropic growth of α-MoO_3. In α-MoO_3, distorted MoO_6 octahedra as interconnect by means of co-edges in [001] bearing (c-axis) and co-vertices in the [100] direction (a-axis). The connection of the neighboring layers in the b-axis relies upon the weak Van der Waals forces. In the event that the MoO_3 crystal develops in the [001] direction, the system will release more energy [20].

The effect of pH (1-9) on h phase MoO_3 was studied as shown in Fig.7 (a-d). When the pH was set to 1, smooth hexagonal rods with different sizes were obtained (Fig.7a). However, when the pH was set to 3, clear hexagonal shaped rods oriented in particular direction (Fig.7b). When the pH was set to 5, these hexagonal rods coalesce together with multi-directions (Fig.7c). However, when the pH was maintained at 9, these hexagonal shaped rods oriented in all the directions and form Bucky ball-like morphology (Fig.7d). Further, the effect of pH on α phase MoO_3 was studied and shown in Fig.7 (e-h). When the pH was maintained at 1 and 3, agglomerated flake-like structures were obtained (Fig.7 e, f). However, when the pH was 5 and 9, agglomerated flakes start separating from each other and finally, a smooth tapered end rods were obtained (Fig.7 g, h).

3.3 Diffuse reflectance (DR) studies

Fig.8 (a) shows the DR spectra of h-MoO_3: Sm^{3+} (1-9 mol %) NSs were recorded at RT in the range of ~ 200-1100 nm. The spectra consist of peaks at ~ 354, 408, 449, 480, 523 and 593 nm, which were due to the transitions of the 4f electrons of Sm^{3+} from the ground-state to $^6H_{5/2} \rightarrow {}^4H_{7/2}$, $^6H_{5/2} \rightarrow {}^4F_{7/2,}$ $^6H_{5/2} \rightarrow {}^4G_{9/2}$, $^6H_{5/2} \rightarrow {}^4I_{11/2}$ and $^6H_{5/2} \rightarrow {}^4F_{3/2}$ transitions, respectively [21]. Further, Kubelka–Munk (K-M) theory was utilized to calculate the energy gap (E_g) of the prepared powders. The Kubelka–Munk function F (R_∞) and photon energy ($h\nu$) was estimated using the relation [22]:

$$F(R_\infty) = \frac{(1-R_\infty)^2}{2R_\infty} \text{ ---------- (6)}$$

$$h\nu = \frac{1240}{\lambda} \text{ ---------- (7)}$$

where R_∞ and λ; the reflection coefficient and absorption wavelength, respectively. The plots of $[F(R_\infty)h\nu]^{1/2}$ versus photon energy ($h\nu$) were shown in the Fig. 8 (b). The estimated E_g values were found to be 3.19-3.34 eV. These values were in good agreement with the reported literature [23].

3.4 Photoluminescence studies

Fig.9 (a, b) shows the excitation and emission spectra of h-MoO_3:Sm^{3+} powders. The PL excitation spectra were recorded by maintaining 610 nm emission wavelengths at room temperature (Fig.9 a). A series of PLE bands at 365 nm ($^6H_{5/2}$–$^4L_{17/2}$), 380 nm ($^6H_{5/2}$–$^6P_{5/2}$), 409 nm ($^6H_{5/2}$–$^4F_{7/2}$), 421 nm ($^6H_{5/2}$–$^6P_{5/2}$), 442 nm ($^6H_{5/2}$–$^4P_{5/2}$), 466 nm ($^6H_{5/2}$–$^4G_{9/2}$), and 483 nm ($^6H_{5/2}$–$^4I_{13/2}$) were observed. Fig. 9(b) shows the emission spectra upon 409 nm

excitation wavelength, consists of the peaks at 563 nm, 610 nm, 647 nm and 698 nm corresponds to the transitions $^4G_{5/2}$–^6H_J (J = 5/2, 7/2, 9/2, 11/2) of Sm^{3+} respectively [24].

Among the peaks, 610 and 563 nm was found to be electric dipole (ED) and magnetic dipole (MD) transitions, respectively [25]. Effect of Sm^{3+} concentration on PL intensity was measured and shown in Fig.9(c). From the figure it was noticed that the highest PL intensity was recorded for 5 mol% of Sm^{3+} and thereafter, it decreases due to concentration quenching [26]. In the present work, the concentration quenching phenomena arise may be due to the energy transfer among dopant Sm^{3+} ions. The critical distance (R_c) between nearby Sm^{3+} ions using following relation [27].

$$R_c \approx 2\left[\frac{3V}{4X_c \pi N}\right]^{1/3} \text{---------- (8)}$$

where V; unit cell volume (Å), N; total Sm^{3+} sites per unit cell and X_c; critical concentration. For the MoO_3: Sm^{3+}system, $N = 4$, $V = 1649(Å)^3$ and $X_c = 0.05$. The estimated value of R_c was found to be ~ 24.44 Å. Hence, it was found that the energy transfers between Sm^{3+} ions take place due to electric multipolar interaction. The schematic representation of Blasse's formula was shown in Fig.10. When critical energy distance between Sm^{3+} ions and MoO_3 was greater than 5 Å; the overlapping between the excitation and emission spectra decreases.

According to Dexter's theory, the type of electric multipolar interaction was estimated by using the following equation [28];

$$\frac{1}{X} = k\left[1+\beta (X)^{Q/3}\right]^{-1} \text{---------- (9)}$$

Where X; Sm^{3+} ion concentration, k and β; constants, Q = 6, 8 and 10 for dipole – dipole, dipole – quadrupole and quadrupole – quadrupole interactions. The value of Q was determined by plotting log (X) *V/s* log (I/X) (Fig.9 (d)), which gives a straight line with a slope = - 0.86155 and intercept = 7.066. The Q value was close to 3, which indicate exchange interaction was the major cause for concentration quenching. The energy level diagram of Sm^{3+} with a cross relaxation mechanism was shown in Fig.9 (e).

3.4. Judd-Ofelt (J-O) analysis

Emission spectrum has been used for the analysis of J-O intensity parameters. The radiative emission rates between $^4G_{5/2}$ and ^6H_J(J=5/2, 7/2, 9/2, 11/2) is given by the relation [29, 30];

$$\frac{I_{0-J}}{I_{0-1}}\frac{h\nu_{0-1}}{h\nu_{0-J}}\cdot\frac{A_{0-J}}{A_{0-1}} = \frac{I_{0-J}}{I_{0-1}}\frac{h\vartheta_{0-1}}{h\vartheta_{0-J}} \text{ ------- (10)}$$

where, I_{0-J}; integrated emission intensities, $h\nu_{0-J}$; photon energies of transitions $^4G_{5/2}\rightarrow{}^6H_J$ (J=5/2, 7/2, 9/2, 11/2). Further, $^4G_{5/2}\rightarrow{}^6H_{5/2}$ corresponds to magnetic dipole (MD) which is independent of crystal field as a result of emission rate/oscillator strength/transition line intensity (A_{0-1}) is a constant (50 s^{-1}) for Sm^{3+} ions. The electric dipole (ED) transition between the excited (J'=0) and lower states (J=5/2, 7/2) is given by the relation [31];

$$A_{0-J} = \frac{64\pi^4 \nu_J^{\,3}}{3h(2J+1)} \frac{n(n^2+2)^2}{9} \sum_{\lambda=2,4} \Omega_\lambda \left| \langle {}^4G_{5/2} \left| U^\lambda \right| {}^6H_J \rangle \right|^2 \quad \text{-------- (11)}$$

The reduced matrix elements value corresponds to the transitions of J=5/2 and 7/2 were found to be 0.0032454 and 0.0023518 respectively. The JO parameters (Ω_2 and Ω_4) for different Sm^{3+} concentrations were estimated by solving the equations 10 and 11.

The other properties namely, A_T (radiative transition probabilities), β_{meas} and β_{calc} (branching ratios), τ_{rad} (radiative lifetime) and asymmetric ratios equivalent to J'=0 and J=5/2 and 7/2 were given by the relations;

$$A_{rad}\left(J^I \rightarrow J\right) = A_{ED} + A_{MD} \quad \text{-------- (12)}$$

$$A_T\left(J^I \rightarrow J\right) = \sum A_{rad}\left(J^I \rightarrow J\right) \quad \text{-------- (13)}$$

$$\beta_{calc} = \frac{A_{rad}\left(J^I \rightarrow J\right)}{A_T\left(J^I \rightarrow J\right)} \quad \text{-------- (14)}$$

$$\beta_{calc} = \frac{\int \lambda I_{J^I J}(\lambda) d\lambda}{\sum_J \int \lambda I_{J^I J}(\lambda) d\lambda} \quad \text{-------- (15)}$$

$$\tau_{rad} = \frac{1}{A_T\left(J^I \rightarrow J\right)} \quad \text{-------- (16)}$$

$$Asymmetricratio = \frac{\int I_{ED} d\lambda}{\int I_{MD} d\lambda} \quad \text{-------- (17)}$$

The obtained results were tabulated in Table 2. The estimated branching ratio were found to be in the range $0.99 \geq 0.50$. The obtained results further validates that the optimized material can effectively utilized in solid state lightening applications. From the table a variation in JO parameters were observed and follow the $\Omega_2 > \Omega_4$ trend. Further, the JO value was found to be higher for 5 mol% Sm^{3+} doped samples which indicate that the influence of the crystal field is

more, as a result the transition $^4G_{5/2} \rightarrow {}^6H_{7/2}$ is found to be greater when compared to $^4G_{5/2} \rightarrow {}^6H_{5/2.}$

Further, the lack of inversion symmetry of Sm^{3+} was confirmed by estimating the value of asymmetric ratio (Table 2).Since the probability of non-radiative transitions was much weaker as a result small variation in branching ratios between the calculated and measured values were observed. The average radiative lifetimes of the samples were estimated and found to be ~ 4.55 ms. The quantum efficiency (η) is estimated based on the relation [32, 33];

$$\eta = \frac{A_R}{A_R + A_{NR}} = \frac{A_R}{A_T} \quad \text{--------- (18)}$$

The estimated values were listed in Table.2. Quantum efficiency (QE) is one of the important parameter in order to access the quality of the prepared phosphor for solid state lightening applications. The QE for $MoO_3:Sm^{3+}$ (1-9 mol %) nanophosphors was estimated by utilizing the relations described by De Mello and Palsson [34, 35]. Both the experimental and theoretical values were in comparisons with each other.The estimated experimental QE values were tabulated in the Table.1. As can be seen from the table it was evident that the highest QE (79.90 %) was observed for5 mol % Sm^{3+} doped MoO_3NSs indicating that the present sample was quite suitable for the display devices.

The assessment and quantification of color is referred to as colorimetry or the 'science of color' [36]. The emission intensities have been characterized by using the CIE 1931 chromaticity diagram. Fig. 11 (a) illustrates the CIE (International Commission onIllumination) chromaticity diagram of $MoO_3:Sm^{3+}$ phosphors for different Sm^{3+} concentrations. CIE parameters such as color coordinates (x, y) and Correlated color temperature (CCT) were calculated to characterize the color emission (Fig. 11 (b)). From the chromaticity diagram, it can be seenthat the color coordinates traversed a narrow range in orange red upon increasing concentration. Observed CIE coordinates were in orange red emission. According to National Television Standard Committee (NTSC) system, the ideal red chromaticity is (0.67, 0.33). The quality of the light source is inspected in terms of the correlated color temperature (CCT) which illustrates the temperature of a closest Plankian black-body radiation to the operating point on the CIE chromaticity diagram [37]. The average CCT (1815 K) for $MoO_3:Sm^{3+}$ has been obtained under 395 nm excitation wavelength. Generally, CCT value greater than 5000 K indicates the coldwhite light used for commercial lighting purpose and lower than 5000 K indicates the warm white light used for

home appliances [38].So, the prepared phosphors were suitable for ideal orange red emission for home appliances. The values of the CIE parameters for thedifferent doped phosphors were summarized in Table 2.

Normally, the light sources can be characterized by their dominant wavelength and color purity of the emitted color. Furthermore, the color purity (CP) of a dominant color is the weight average of the (x, y) coordinate relative to the coordinate of the dominant wavelength and the coordinate of the CIE white illumination [39]. In this case a single monochromatic dominant wavelength corresponds to 610 nm to the CIE coordinate. The CP was estimated based on the well-known relation [40];

$$color\ \ purity = \frac{\sqrt{(x_s - x_i)^2 + (y_s - y_i)^2}}{\sqrt{(x_d - x_i)^2 + (y_d - y_i)^2}} \times 100\% \quad \text{---------- (20)}$$

Where x_s= 0.572, y_s = 0.427 were the color coordinate of the light source, x_i= 0.3333, y_i=0.3333, were the CIE white illuminant and x_d= 0.67, y_d = 0.33 were the chromaticity coordinate corresponding to the dominant wavelength (610 nm) point. By substituting all the values in eqn. 20, finally the average CP was obtained for MoO_3:Sm^{3+} is found to be ~97%. The estimated values were tabulated in Table 2. The results indicate that color purity was high in prepared phosphors and ideal orange red chromaticity with high color purity and therefore has promising applications in solid-state lighting and display devices [41].

4. Conclusions

Hexagonal and orthorhombic phase of MoO_3 NSs were prepared by simple hydrothermal route. The surface morphology of the product was highly dependent on reaction temperature, time and lysine concentration. At 240 ^oC h- MoO_3 phase was noticed. The energy band gap values were found to increase with dopant concentration. The emission spectra exhibit a series of peaks at 563 nm, 610 nm, 647 nm and 698 nm corresponds to the transitions $^4G_{5/2}$–^6H_J (J = 5/2, 7/2, 9/2, 11/2) of Sm^{3+} respectively. The PL emission intensity was found to enhance upto 5 mol % of Sm^{3+} ions and thereafter it decreases. The JO intensity parameters (Ω_2>Ω_4) confirms the covalency between the metal and ligands as well as the asymmetry around Sm^{3+} ions. The photometric results indicate that the phosphor emit orange-red light which was quite useful for the production of artificial white light for display device applications.

References

1. W.Xie, J.Feng, X. Liu, L. Yan, H.Guo, Y.Dai, Y.Xie, H.S. Jang, J. Lin, Multi-color luminescence evolution of $SrGdAlO_4:Ln^{3+}$ (Ln^{3+} = Eu^{3+} and/or $Tb^{3+)}$ nanocrystalline phosphors via a sol-gel process, J. Alloys Compd., 753 (2018) 781-790.
2. P.Solarz, M.Głowacki, M.Berkowski, W. Ryba-Romanowski, Growth and spectroscopy of $Gd_3Ga_3Al_2O_{12}$ (GGAG) and evidence of multisite positions of Sm^{3+} ions in solid solution matrix, J. Alloys Compd., 689 (2016) 359-365.
3. Yong-Ping Gao, Ke-Jing Huang, Chen-Xi Zhang, Shuai-Shuai Song, Xu Wu, High-performance symmetric supercapacitor based on flower-like zinc molybdates, J. Alloys Compd., 731 (2018) 1151-1158.
4. Frederick Nti, Daniel AdjahAnang, Jeong In Han, Facilely synthesized $NiMoO_4/CoMoO_4$ nanorods as electrode material for high performance supercapacitor, J. Alloys Compd., 742 (2018) 342-350.
5. Liyun Cao, Yan Li, Jianpeng Wu, Wenbin Li, Jianfeng Huang, YongqiangFeng, Chunyan Yao, Jiayin Li, Ruiyi Wang, Qian Kang, LiangliangFeng, Facile synthesis of carbon coated MoO_3 nanorods decorated with WO_2 nanoparticles as stable anodes for lithium-ion batteries, J. Alloys Compd., 744 (2018) 672-678.
6. H.S. Yogananda, H. Nagabhushana, G.P. Darshan, R.B. Basavaraj, B. Daruka Prasad, M.K. Sateesh, G.K. Raghu, MoO_3 nanostructures from EGCG assisted sonochemical route: Evaluation of its application towards forensic and photocatalysis, J. Alloys Compd., 745 (2018) 874-891.
7. H.S. Yogananda, H. Nagabhushana, Ramachandra Naik, S.C. Prashantha, Calcination temperature dependent structural modifications, tailored morphology and luminescence properties of MoO_3 nanostructures prepared by sonochemical method, J. Sci.: Adv. Mater. Devices., 3 (2018) 77-85.
8. Ahmed S. Etman, Hani Nasser Abdelhamid, Youyou Yuan, Ligang Wang, XiaodongZou, Junliang Sun, Facile Water-Based Strategy for Synthesizing MoO_{3-x} Nanosheets: Efficient Visible Light Photocatalysts for Dye Degradation, ACS Omega, 3 (2018) 2193-2201.
9. M. Layegh, F.E. Ghodsi, H. Hadipour, Improving the electrochemical response of nanostructured MoO_3 electrodes by Co doping: Synthesis and characterization, J. Phys. Chem. Solids, 121 (2018)375-385.
10. J. Bolitschek, S. Luidold, M. O'Sullivan, A study of the impact of reduction conditions on molybdenum morphology, Int. J. Refract. Met. Hard Mater., 71 (2018) 325-329.
11. Yosep Han, YoungwooRheem, Kyu-Hwan Lee, Hyunjung Kim, Nosang V. Myung, Synthesis and characterization of orthorhombic-MoO_3 nanofibers with controlled morphology and diameter, J. Ind. Eng. Chem., 62 (2018) 231-238.
12. Baosheng Cao, Xuehan Wang, Luis Rino, Jinlei Wu, Yangyang He, ZhiqingFeng, BinDong, Morphology and upconversion properties of rare-earth-doped MoO_3 jellyfish-like plate microarchitecture, Mater. Lett., 213 (2018) 4-6.
13. A. A. Mane, A. V. Moholkar, Orthorhombic MoO_3nanobelts based NO_2 gas sensor, Appl. Surf. Sci., 405 (2017) 427-440.
14. N. Guru Prakash, M. Dhananjaya, A. Lakshmi Narayana, Dadamiah PMD Shaik, P. Rosaiah, O.M. Hussain, High Performance One Dimensional α-MoO_3 Nanorods for Supercapacitor Applications, Ceram. Int., 44 (2018) 9967-9975.

15. PitchaiThangasamy, VadivelShanmugapriya, MarappanSathish, One-dimensional growth of hexagonal rods of metastable h-MoO_3 using one-pot, rapid and environmentally benign supercritical fluid processing, Physica E., 99 (2018) 189-193.
16. Juan C. Icaza, Richard T. Haasch, Ramesh K.Guduru, Effect of ion size and charge density on the electrochemical characteristics of α-MoO_3 using aqueous Be^{2+} and Mg^{2+} sulfate electrolytes, J. Alloys Compd., 740 (2018) 88-95.
17. R.B. Basavaraj, H. Nagabhushana, G.P. Darshan, B. Daruka Prasad, M. Rahul, S.C. Sharma, R. Sudaramani, K.V. Archana, Red and green emitting CTAB assisted $CdSiO_3$: Tb^{3+}/Eu^{3+} nanopowders as fluorescent labeling agents used in forensic and display applications, Dyes Pigm. 147 (2017) 364-377.
18. A. Khorsand Zak, W.H. Abd. Majid, M.E. Abrishami, RaminYousefi, X-ray analysis of ZnO nanoparticles by Williamson-Hall and size-strain plot Methods, Solid State Sci., 13 (2011)251-256.
19. R.B. Basavaraj, H. Nagabhushana, B. Daruka Prasad, S.C. Sharma, K.N. Venkatachalaiah, Mimosa pudica mediated praseodymium substituted calcium silicate nanostructures for white LED application, J. Alloys Compd. 690 (2017) 730-740.
20. Woosun Jang, Jongmin Yun, Taehun Lee, Yonghyuk Lee, Aloysius Soon, Disentangling the Effects of Inter- and Intra-octahedral Distortions on the Electronic Structure in Binary Metal Trioxides, J. Phys. Chem. C, 122 (2018) 3558-3566.
21. XiaoyongHuang, HengGuo, $LiCa_3MgV_3O_{12}$:Sm^{3+}: A new high-efficiency white-emitting phosphor, Ceram. Int., 44 (2018) 10340-10344.
22. R.B. Basavaraj, H. Nagabhushana, B. Daruka Prasad, G.R. Vijayakumar, Zinc silicates with tunable morphology by surfactant assisted sonochemical route suitable for NUV excitable white light emitting diodes, Ultrason. Sonochem., 34 (2017) 700-712.
23. A. Bouzidi, N. Benramdane, H. Tabet-Derraz, C. Mathieu, B. Khelifa, R. Desfeux, Effect of substrate temperature on the structural and optical properties of MoO3 thin films prepared by spray pyrolysis technique, Mater. Sci. Eng., B. 97 (2003) 5-8.
24. C. Suresh, H. Nagabhushana, G.P. Darshan, R.B. Basavaraj, D. Kavyashree, S.C. Sharma, A. Arulmozhi, B. Daruka Prasad, H.J. Amith Yadav, Facile LaOF: Sm^{3+} based labeling agent and their applications in residue chemistry of latent fingerprint and cheiloscopy under UV–visible light, Arabian J. Chem., 11 (2018) 460-482.
25. G. Ramakrishna, H. Nagabhushana, R.B. Basavaraj, S.C. Prashantha, S.C. Sharma, Ramachandra Naik, K.S. Anantharaju, Green synthesis, structural characterization and photoluminescence properties of Sm^{3+} co-doped Y_2SiO_5:Ce^{3+} nanophosphors for wLEDs, Optik., 127 (2016) 5310-531.
26. R.B. Basavaraj, H. Nagabhushana, B. Daruka Prasad, S.C. Sharma, S.C. Prashantha, B.M. Nagabhushana, A single host white light emitting Zn_2SiO_4:Re^{3+} (Eu, Dy, Sm) phosphor for LED applications, Optik., 126 (2015) 1745-1756.
27. R.B. Basavaraj, H. Nagabhushana, G.P. Darshan, B. Daruka Prasad, S.C. Sharma, K.N. Venkatachalaiah, Ultrasound assisted rare earth doped Wollastonite nanopowders: Labeling agent for imaging eccrine latent fingerprints and cheiloscopy applications, J. Ind. Eng. Chem. 51 (2017) 90-105.
28. B. Marappa, M.S. Rudresha, R.B. Basavaraj, G.P. Darshan, B. Daruka Prasad, S.C. Sharma, S. Sivakumari, P. Amudha, H. Nagabhushana, EGCG assisted Y_2O_3:Eu^{3+} nanopowders with 3D micro-architecture assemblies useful for latent finger print recognition and anti-counterfeiting applications, Sens. Actuators, B, 264 (2018) 426-439.
29. D. Navami, R.B. Basavaraj, S.C. Sharma, B. Daruka Prasad, H. Nagabhushana, Rapid identification of latent fingerprints, security ink and WLED applications of $CaZrO_3$:Eu^{3+} fluorescent labelling agent fabricated via bio-template assisted combustion route, J. Alloys Compd., 762 (2018) 763-779.

30. C. Suresh, H. Nagabhushana, R.B. Basavaraj, G.P. Darshan, D. Kavyashree, B. Daruka Prasad, S.C. Sharma, R. Vanithamani, SiO_2@LaOF:Eu^{3+} core-shell functional nanomaterials for sensitive visualization of latent fingerprints and WLED applications, J. Colloid Interface Sci. 518 (2018) 200-215.
31. C. Suresh, H. Nagabhushana, R.B. Basavaraj, G.P. Darshan, D. Kavyashree, B. Daruka Prasad, S.C. Sharma, R. Vanithamani, SiO_2@LaOF:Eu^{3+} core-shell functional nanomaterials for sensitive visualization of latent fingerprints and WLED applications, J. Colloid Interface Sci., 518 (2018) 200-215.
32. M. Venkataravanappa, R.B. Basavaraj, G.P. Darshan, B. Daruka Prasad, S.C. Sharma, P. HemaPrabha, S. Ramani, H. Nagabhushana, Multifunctional Dy (III) doped di-calcium silicate array for boosting display and forensic applications, J. Rare Earths., 36 (2018) 690-702.
33. KanchanMondal, Puja Kumari, J. Manam, Influence of doping and annealing temperature on the structural and optical properties of Mg_2SiO_4:Eu^{3+} synthesized by combustion method, Curr. Appl Phys., 16 (2016) 707-719.
34. J.C. De Mello, H.F. Wittmann, R.H. Friend, An improved experimental determination of external photoluminescence quantum efficiency, Adv. Mater. 9 (1997) 230-232.
35. L.O. Palsson, A.P. Monkman, Measurements of Solid-State Photoluminescence Quantum Yields of Films Using a Fluorimeter, Adv. Mater. 14 (2002) 757-758.
36. JianghuiZheng, Lili Ying, Qijin Cheng, ZiquanGuo, LihanCai, Yijun Lu,Chao Chen, Blue-emitting SrB_2O_4:Eu^{2+} phosphor with high color purity for near-UV white light-emitting diodes, Mater. Res. Bull., 64 (2015) 5-54.
37. Publication CIE no 17.4 (1987) International Lighting Vocabulary, Central Bureau of the Commission Internationale de L 'Eclairage, Vienna, Austria.
38. S. Som, Vijay Kumar, Vinod Kumar, M. Gohain, A. Pandey, M.M. Duvenhag, J.J. Terblans, B.C.B. Bezuindenhoud, H.C. Swart, Dopant distribution and influence of sonication temperature on the pure red light emission of mixed oxide phosphor for solid state lighting, Ultrason. Sonochem., 28 (2016) 79-89.
39. SumandeepKaur, A.S. Rao, M. Jayasimhadri, Enhanced red down-conversion luminescence and high color purity from flux assisted Eu^{3+} doped calcium aluminozincate phosphor, J. Lumin., 202 (2018) 461-468.
40. Yang Li, JianghuiZheng, Zhen Li, Xing Yang, Jiachao Chen, Chao Chen, Luminescence properties of $NaSrPO_4$: Tm^{3+} as novel blue emitting phosphors with high color purity, Optik, 169 (2018) 257-263.
41. Peng Chen, WenyuanHu, Dingming Yang, Jiayi Zhu, Jing Zhang, YadongWu, Ba_2ZnWO_6:Sm^{3+} as promising orange-red emitting phosphors: Photoluminescence properties and energy transfer process, Physica B., 530 (2018) 127-132.

Figures:

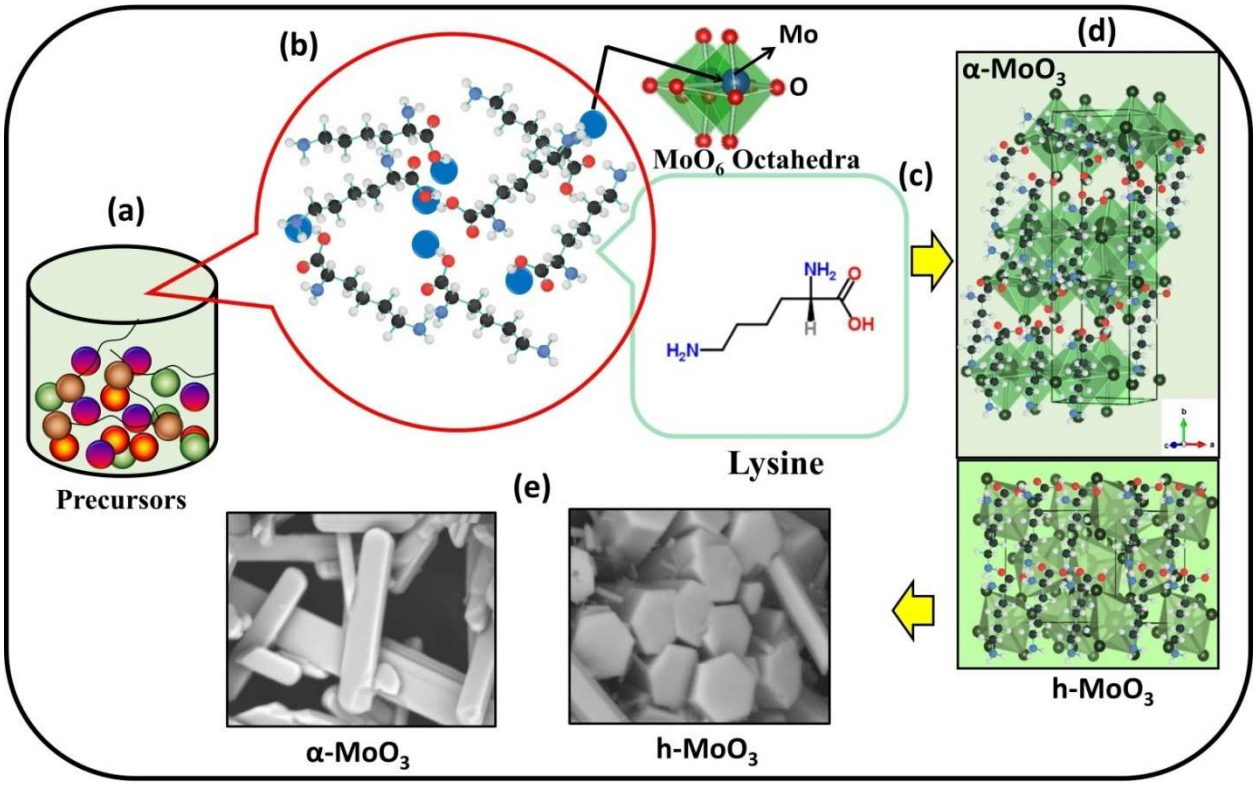

Fig. 1.Schematic diagram of synthesis of MoO_3, its structure and morphological behavior.

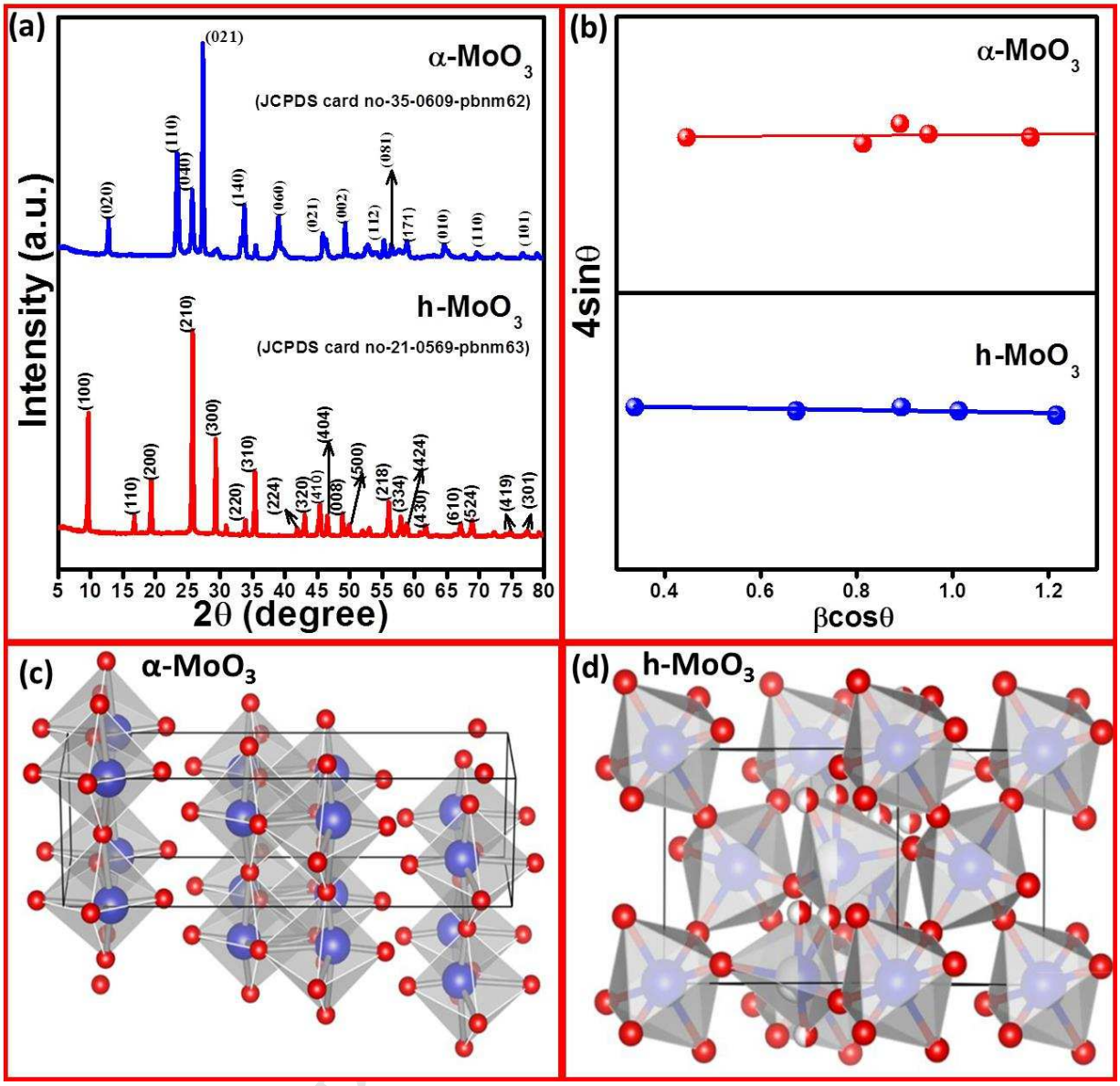

Fig.2. (a) PXRD patterns of un-doped MoO_3. (b) W-H patterns of un-doped MoO_3. (c) Crystal structures of α- MoO_3 and (d) h- MoO_3.

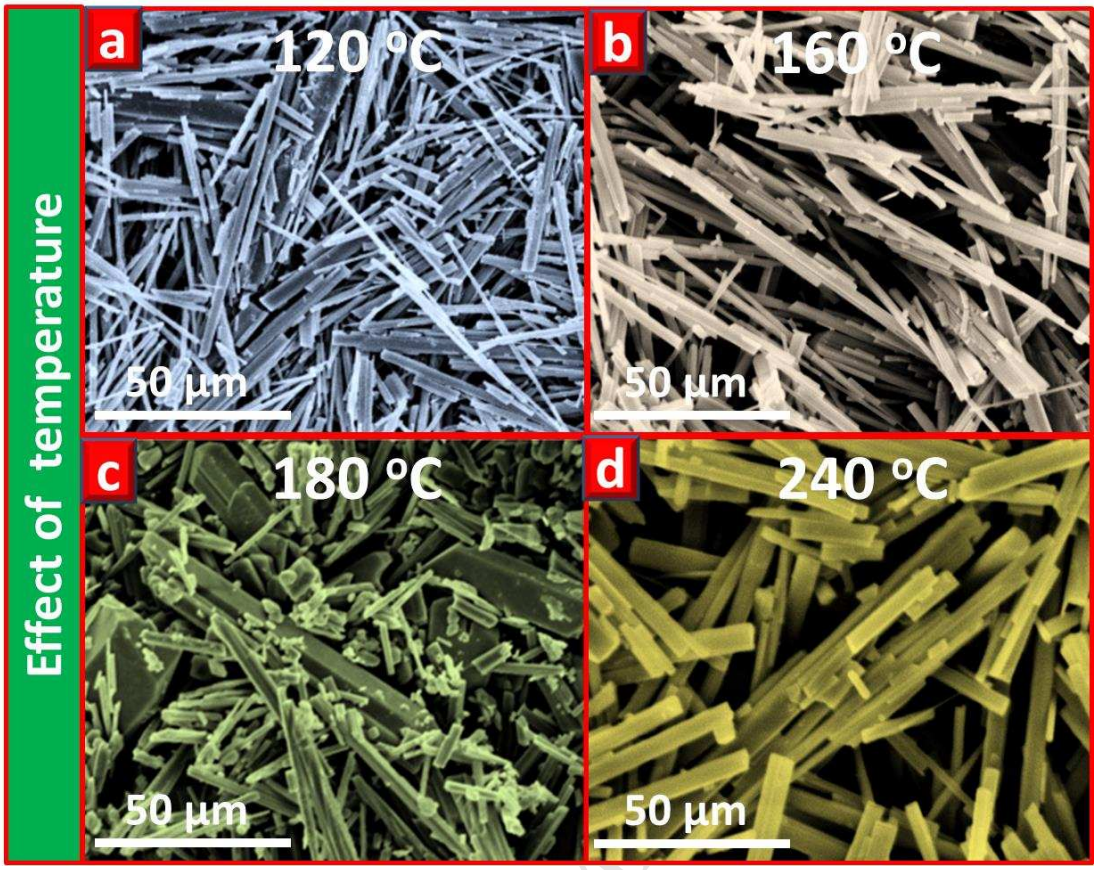

Fig.3. SEM images ofα-MoO_3 with different temperatures.

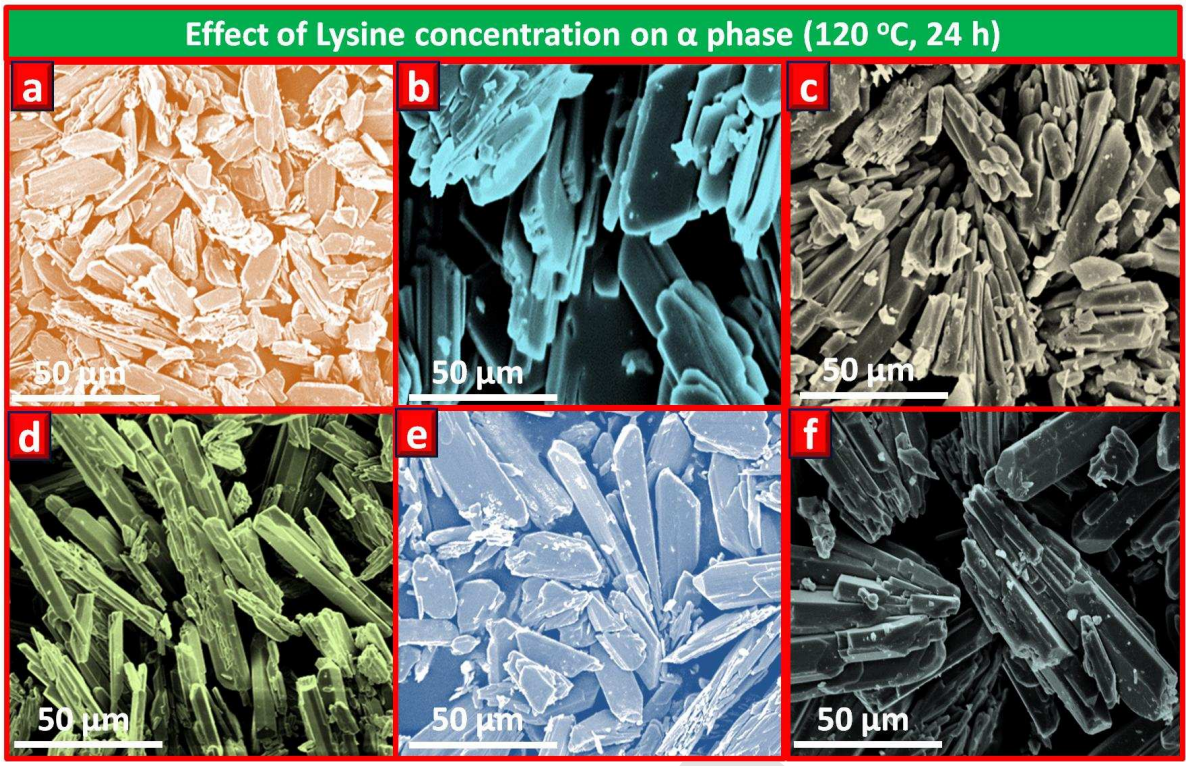

Fig.4. SEM images of α- MoO_3 at 120 ^{o}C with different concentrations of lysine (a) 0.5 g, (b) 1 g, (c) 1.5 g, (d) 2 g, (e) 2.5 g, (f) 3 g.

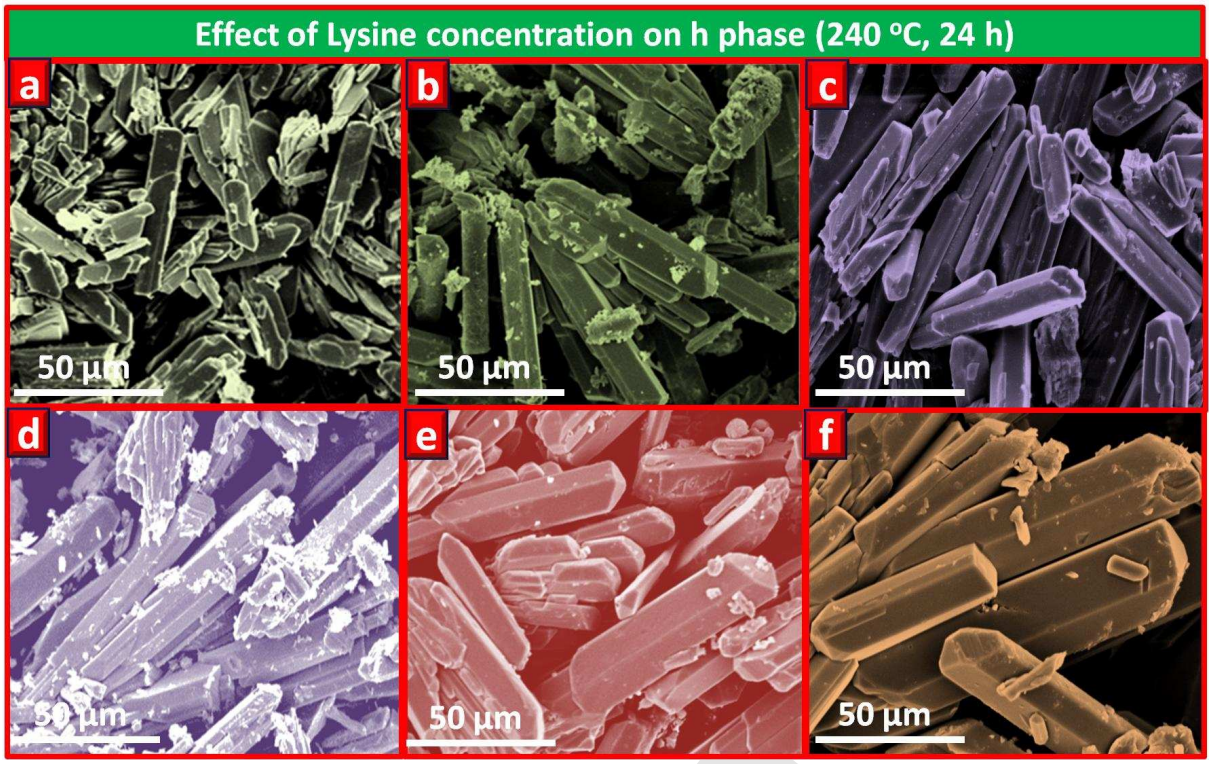

Fig.5. SEM images of h- MoO_3 at 240 ^{o}C with different concentrations of lysine (a) 0.5 g, (b) 1 g, (c) 1.5 g, (d) 2 g, (e) 2.5 g, (f) 3 g.

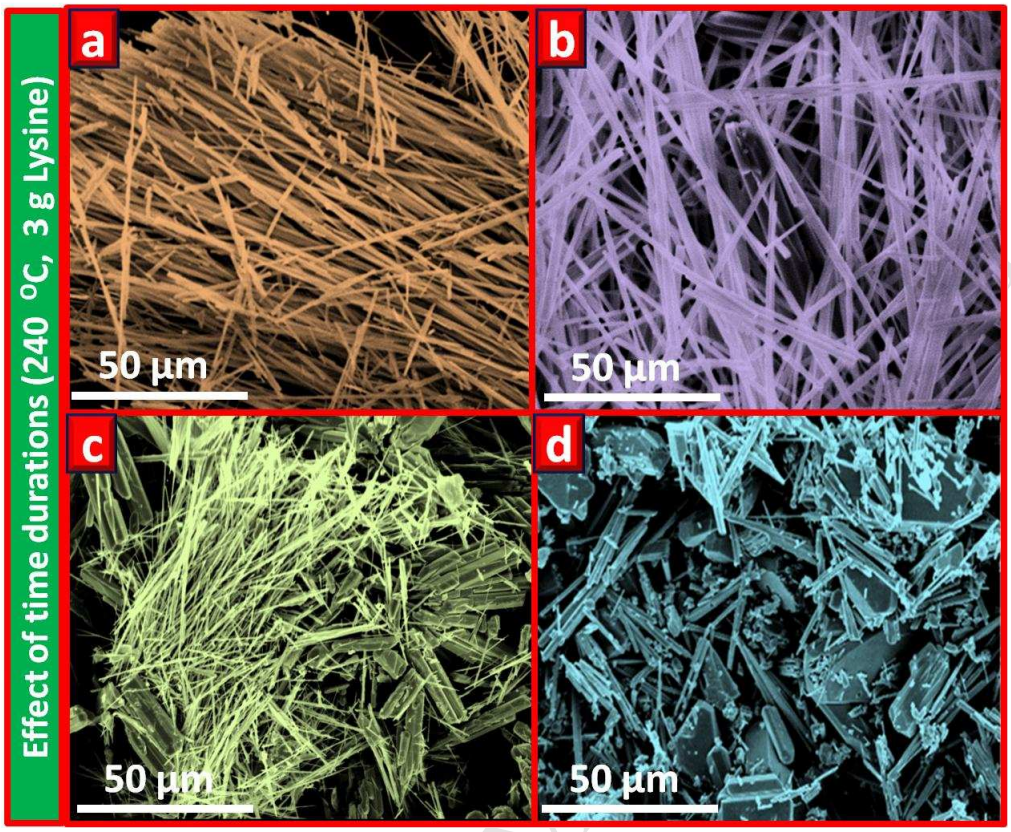

Fig.6. SEM images of 3 g lysine treated samples at different time durations (a) 4 h, (b) 8 h, (c) 12 h, (d) 16 h at 240 ^{o}C.

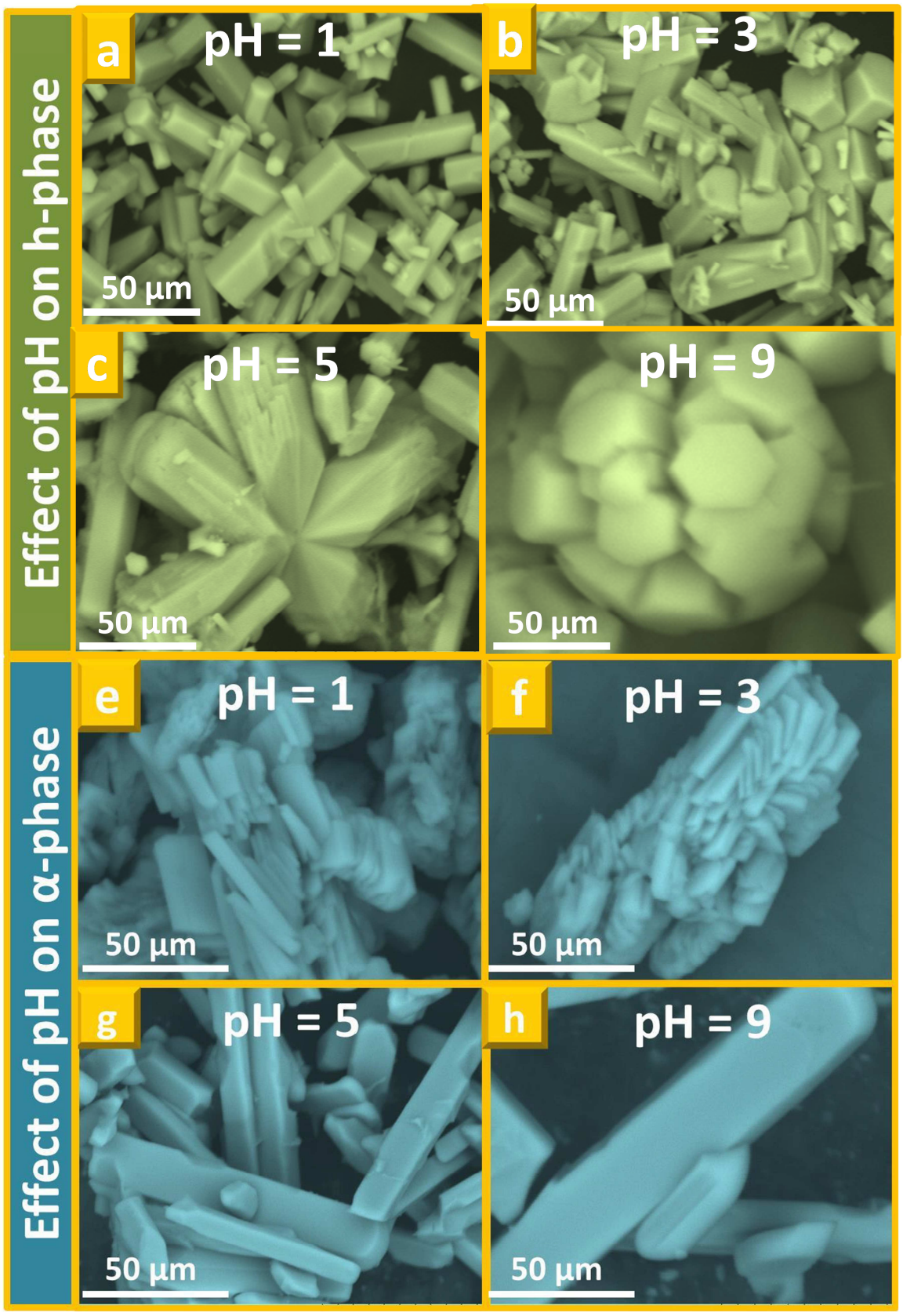

Fig.7. SEM images of α- MoO_3 and h- $MoO_3$with different pH values.

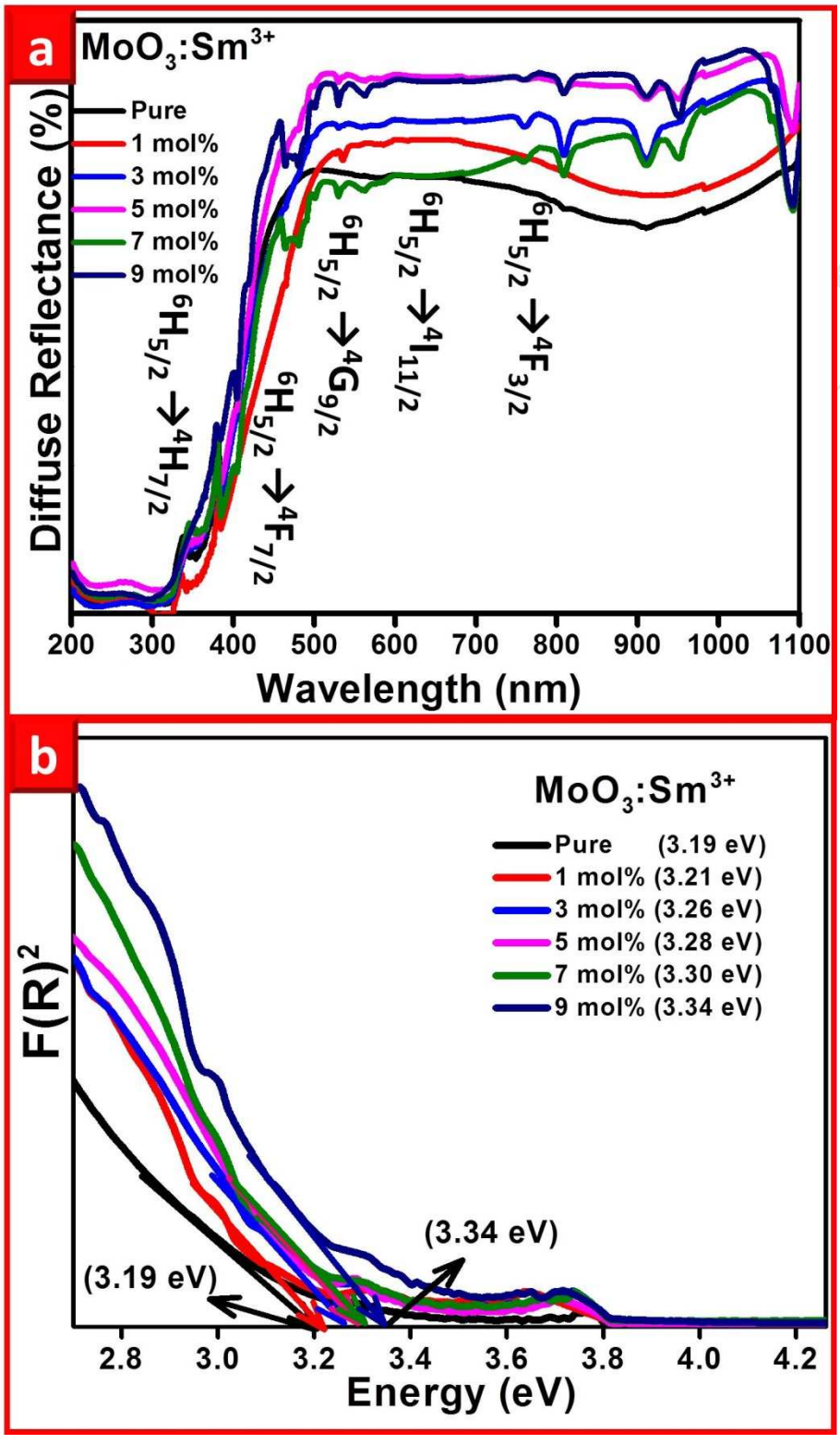

Fig.8. (a) diffuse reflectance spectra and (b) band gap plots of Sm^{3+} doped MoO_3NSs.

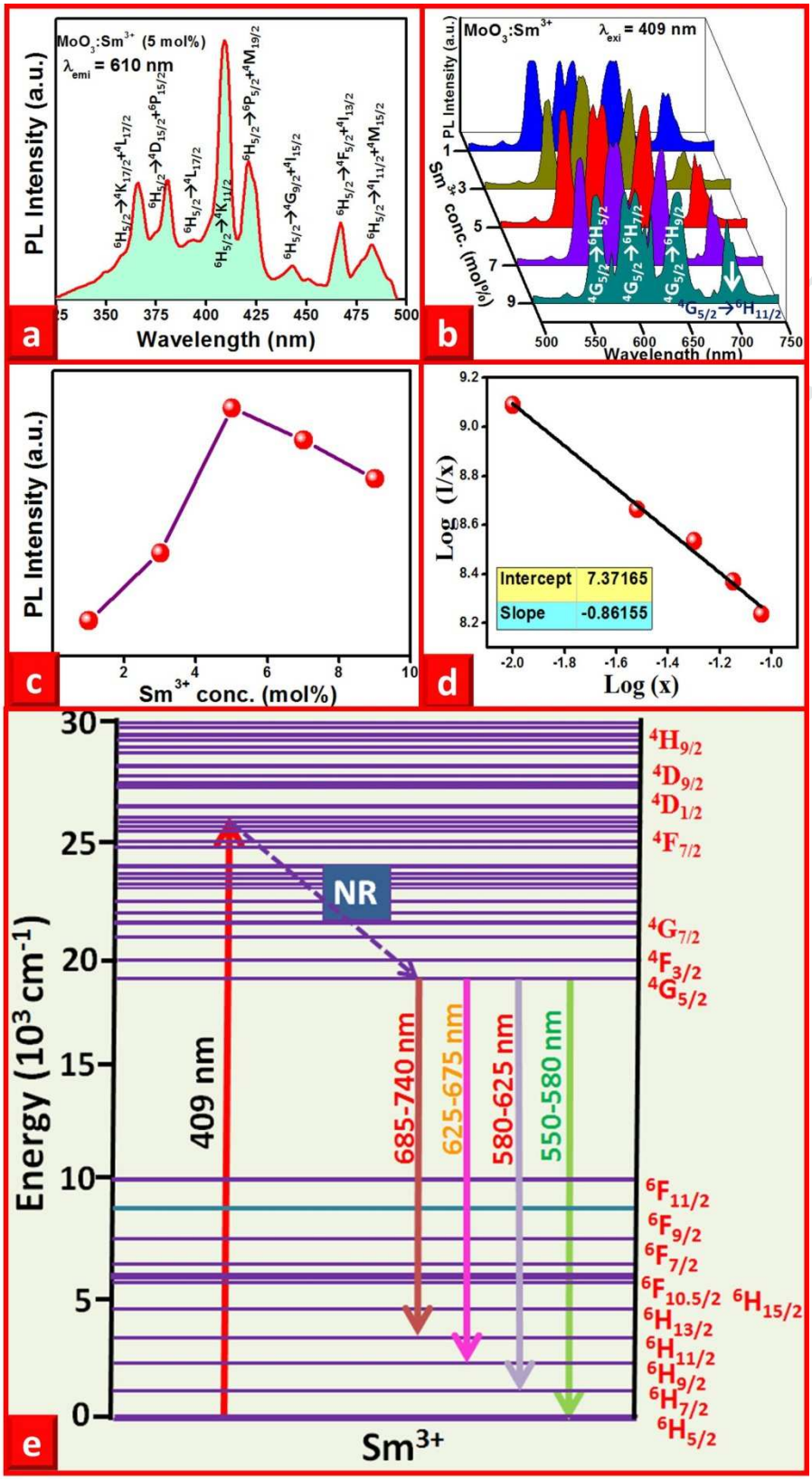

Fig.9. (a) Excitation spectrum, (b) emission spectra, (c) variation of PL intensity with Sm^{3+} concentration, (d) Relation between log(x) and log (I/x) in Sm^{3+} doped MoO_3 nanophosphors.(e) energy level diagram of Eu^{3+} ions.

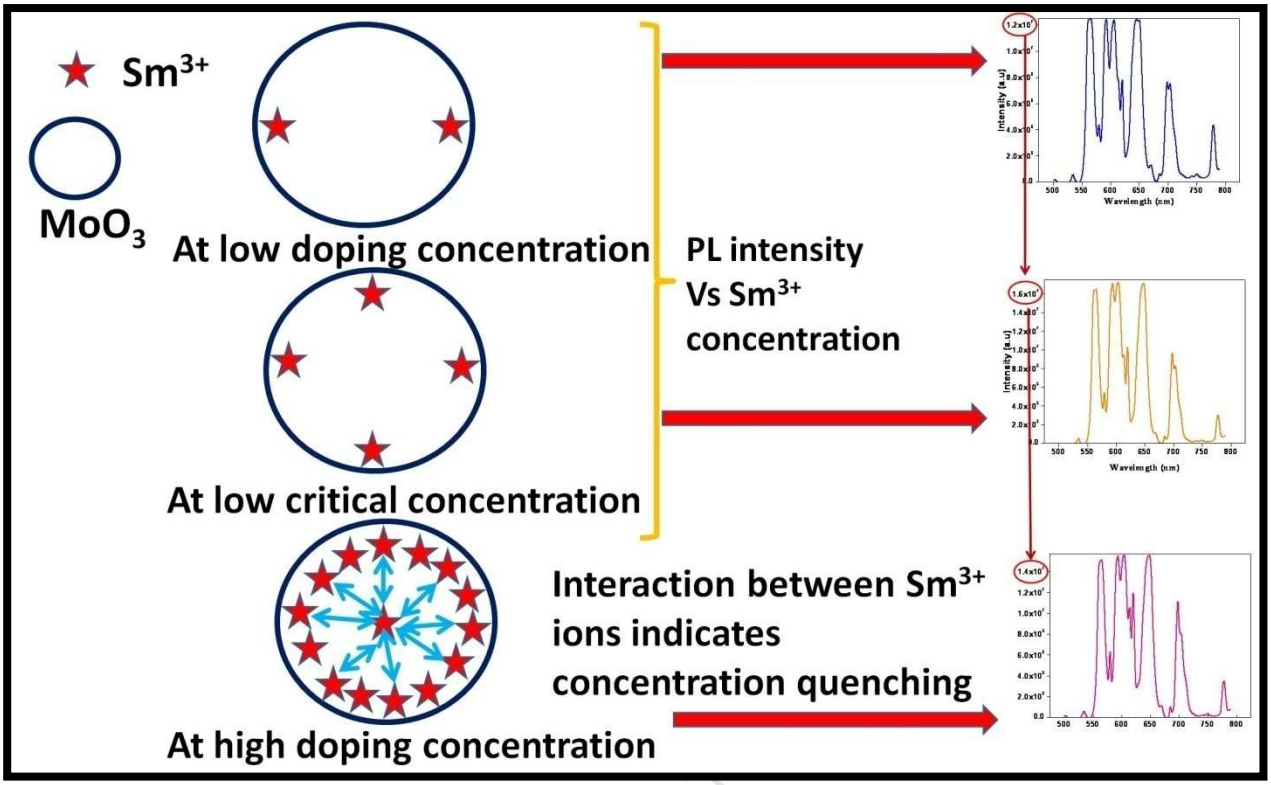

Fig.10. Schematic representation energy transfer and concentration quenching.

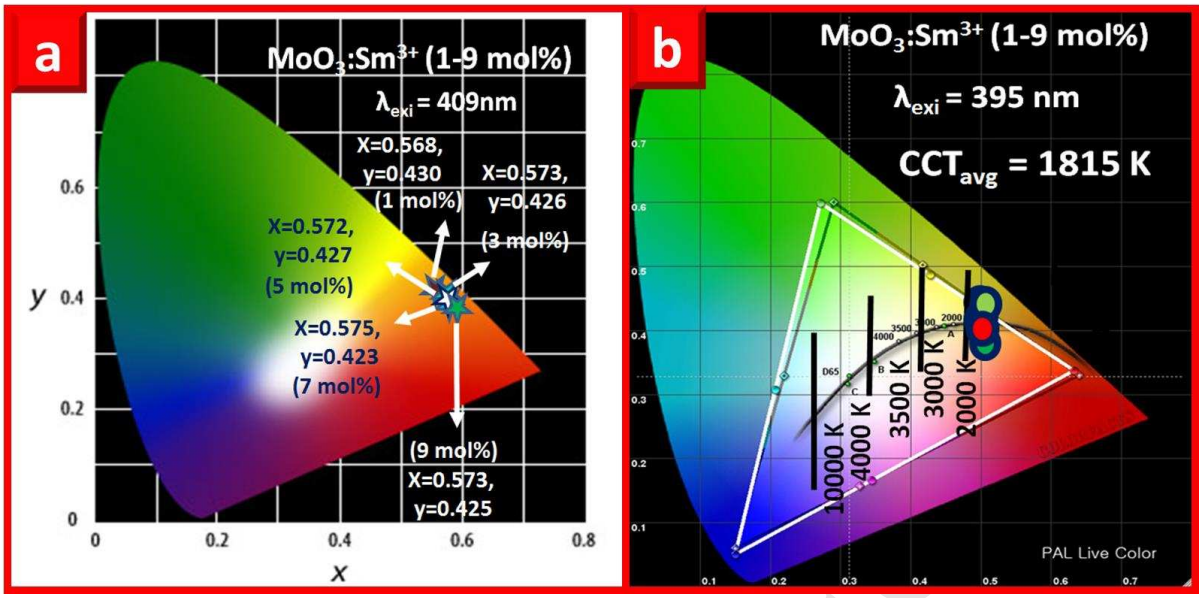

Fig.11 (a) CIE and (f) CCT diagrams of $MoO_3:Sm^{3+}$ NSs.

Table.1. Judd-Ofelt intensity parameters (Ω_2, Ω_4), radiative transition probability (A_T), calculated radiative (τ_{rad}) lifetime, branching ratio (β_R), asymmetric ratio (A_{21}) and quantum efficiency (η) of MoO_3: Sm^{3+}NSs.

Sm^{3+} con. (mol %)	Judd-Ofelt intensity parameters ($\times 10^{-20}$ cm^{-1})		Transitions	A_{ED} (S^{-1})	A_{MD} (S^{-1})	$A_{rad} = A_{ED} + A_{MD}$	β_{meas}	β_{calc}	τ_{rad} (ms)	Asymmetric ratio	A_T (s^{-1})	η (%)	η_{exp} (%)
	Ω_2	Ω_4											
1	2.31	1.32	$^4G_{5/2} \rightarrow {}^6H_{5/2}$	-	50	50	0.218	0.216	4.37	2.35	228	79.72	78.23
			$^4G_{5/2} \rightarrow {}^6H_{7/2}$	117.90	-	117.90	0.516	0.512					
			$^4G_{5/2} \rightarrow {}^6H_{9/2}$	60.57	-	60.57	0.265	0.270					
3	2.37	1.37	$^4G_{5/2} \rightarrow {}^6H_{5/2}$	-	50	50	0.250	0.245	4.01	2.97	199	79.58	79.45
			$^4G_{5/2} \rightarrow {}^6H_{7/2}$	98.82	-	98.82	0.495	0.491					
			$^4G_{5/2} \rightarrow {}^6H_{9/2}$	50.77	-	50.77	0.254	0.250					
5	2.48	1.48	$^4G_{5/2} \rightarrow {}^6H_{5/2}$	-	50	50	0.244	0.248	4.88	2.04		79.26	79.11
			$^4G_{5/2} \rightarrow {}^6H_{7/2}$	102.16	-	102.16	0.499	0.495			204		
			$^4G_{5/2} \rightarrow {}^6H_{9/2}$	52.48	-	52.48	0.256	0.250					
7	2.37	1.36	$^4G_{5/2} \rightarrow {}^6H_{5/2}$	-	50	50	0.229	0.230	4.58	2.22		79.61	78.45
			$^4G_{5/2} \rightarrow {}^6H_{7/2}$	111.03	-	111.03	0.509	0.510			218		
			$^4G_{5/2} \rightarrow {}^6H_{9/2}$	57.04	-	57.04	0.261	0.265					
9	2.24	1.25	$^4G_{5/2} \rightarrow {}^6H_{5/2}$	-	50	50	0.245	0.240	4.91	2.03	203	79.90	79.85
			$^4G_{5/2} \rightarrow {}^6H_{7/2}$	101.50	-	101.50	0.498	0.490					
			$^4G_{5/2} \rightarrow {}^6H_{9/2}$	52.15	-	52.15	0.256	0.251					

Table.2. Photometric characteristics of MoO_3: Sm^{3+} (1- 9 mol %)NSs.

Sm^{3+} mol%	**CIE Coordinates**		**CCT values**		**CCT (K)**	**CP %**
	x	**y**	**u'**	**v'**		
1	0.568	0.430	0.3777	0.4320	1823	96.3
3	0.573	0.426	0.3324	0.4932	1759	97.8
5	0.572	0.427	0.3509	0.459	1984	96.3
7	0.575	0.423	0.3335	0.4773	1749	98.8
9	0.573	0.425	0.3606	0.4635	2123	98.4

Research highlights

- MoO_3: Sm^{3+} prepared using hydrothermal method.
- Heirarchical SEM were analyzed.
- PL and photometric studies were carried out.